# Investigation of the Sound Source Regions in Open and Closed Organ Pipes

Viktor HRUŠKA*, Pavel DLASK

*Academy of Performing Arts in Prague*
*Music Acoustics Research Centre*
Prague, Czech Republic
*Corresponding Author e-mail: hruska.viktor@hamu.cz

The airflow in the mouth of an open and closed flue organ pipe of corresponding geometrical proportions is studied. The phase locked particle image velocimetry with subsequent analysis by the biorthogonal decomposition is employed in order to compare the flow mechanisms and related features. The most significant differences lie in the mean velocity distribution and rapidity of the jet lateral motion. Remarks on the pressure estimation from PIV data and its importance for the aeroacoustic source terms are made and a specific example is discussed.

**Keywords:** particle image velocimetry; acoustics of music instruments; organ pipes; edge aerophones.

## 1. Introduction

Open and closed (stopped) flue organ pipes are probably the most widely renown examples of half wavelength and quarter wavelength resonators along with the typical sound spectra. We focus on the comparative study of the airflow in the mouth of a closed and open pipe using the particle image velocimetry (PIV). Such comparison has not been published to our best knowledge yet.

Much work has been done on the subject of airflow in the mouth of the pipe (see (CHAIGNE, KERGOMARD, 2016; FABRE *et al.*, 2012; FLETCHER, ROSSING, 1998) for review and summary). The particle image velocimetry (PIV) is a standard technique nowadays, hence there is no need to describe its features and capabilities for music acoustics in details (see e.g. YOSHIKAWA *et al.*, 2012; HRUŠKA, DLASK, 2017; MICKIEWICZ, 2015; MACDONALD, 2009; BAMBERGER, 2008).

Source terms of the wave equations predicted by the aeroacoustic analogies (HOWE, 2002; HIRSCHBERG, RIENSTRA, 2004, UOSUKAINEN, 2011) demand evaluation of the 2nd derivatives of the velocity field which is applicable on the data from numerical simulations (see e.g. MIYAMOTO *et al.*, 2013). However, it is doubtful in our case due to the measurement uncertainties (see below). An alternative and very useful approach relies on the calculation of the acoustic power generated by the unsteady flow. Recall that the velocity field $\mathbf{u}$ can be decomposed by means of the scalar and vector potential to the curl free $\phi$ and divergence free $\mathbf{\Psi}$ parts as $\mathbf{u} = \nabla \left( \phi_0 + \phi' \right) + \nabla \times \mathbf{\Psi}$, where the zero subscript and the prime denote steady and unsteady parts of the velocity potential respectively. The acoustic velocity $\mathbf{u}_{ac}$ is defined using the unsteady component of the potential flow $\mathbf{u}_{ac} = \nabla \phi'$. By the Howe's formula (or the Howe's energy corollary) the mean acoustic power $\langle \mathcal{P} \rangle$ generated or dissipated in a control volume $\Omega$ could be expressed as (HOWE, 1975; LIN, POWELL, 1998; CHAIGNE, KERGOMARD, 2016):

$$\langle \mathcal{P} \rangle = - \left\langle \int_\Omega \rho_0 \left( \boldsymbol{\omega} \times \mathbf{u} \right) \cdot \mathbf{u}_{ac} \, \mathrm{d}\Omega \right\rangle, \qquad (1)$$

where $\boldsymbol{\omega} \equiv \nabla \times \mathbf{u}$ is the vorticity and $\rho_0$ the ambient density. This approach has been applied before, notably by YOSHIKAWA *et al.* (2012). Nevertheless, such procedure requires knowledge of the acoustic velocities distribution in the investigated domain which is not available from the complex flow measurement. Hence we focus on the acoustic synchronised flow dynamics and make some remarks on the further aeroacoustic investigation in the discussion.

The paper is organised as follows. First the measurement setup and employed methods are introduced. Then the results of the PIV measurement alongside with their interpretation and biorthogonal decomposition analysis are presented. The discussion deals

with the experimental and post processing issues and brings the topic of pressure assessment based on PIV data. The paper is completed with conclusions.

## 2. Measurement setup and methods

A transparent organ pipe was used for PIV measurements (see Fig. 1). Its construction enables both an open end configuration and a closed one. The parameters are summarised in Table 1 and the geometry visualised in Fig. 2. For the sake of comparability the same blowing conditions were chosen for both configurations (where possible).
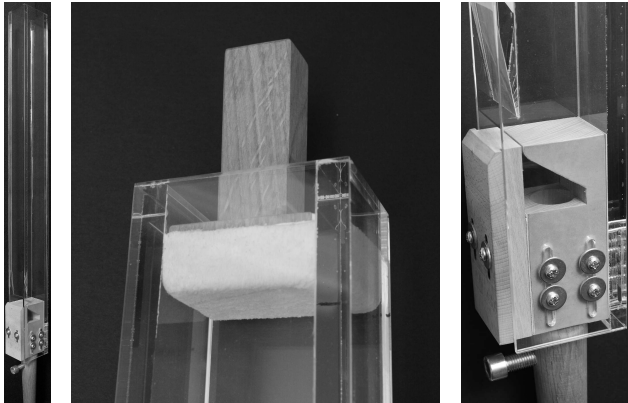


Fig. 1. Transparent pipe used for experiments (left), detail of the stopper (middle), detail of the mouth (right).

Table 1. Summary of the pipe parameters. The length is given without corrections due to the open end and mouth radiation effects (i.e., the length is a pure geometrical distance block – open end or block – stopper).

|  | Open pipe | Closed pipe |
|---|---|---|
| Length [mm] | 718 | 679 |
| Cut up [mm] | 18 | 18 |
| Flue width [mm] | 1.6 | 1.6 |
| Pipe cross section [mm$^2$] | 2475 | 2475 |
| Mouth cross section [mm$^2$] | 810 | 810 |
| Windchest pressure [Pa] | 600 | 600 |
| Foot pressure [Pa] | 100 | 100 |
| Mean flue velocity [m/s] | 14 | 14 |
| SPL [dB] at 1 m | 86 | 80 |

The mean flue velocity was obtained from the PIV data just above the flue. It is common to give the windchest pressure as an organ voicing input parameter although the mean flue velocity does not correspond to it. According to the usual Bernoulli approximation $u_{jet} = \sqrt{2\Delta p/\rho_0}$ the velocity should be considerably higher. The reason is that the foot bore is significantly constricted by the screw (see Fig. 1). The actual blowing pressure inside the foot is only 100 Pa, which gives a suitable correspondence with the Bernoulli approximation.
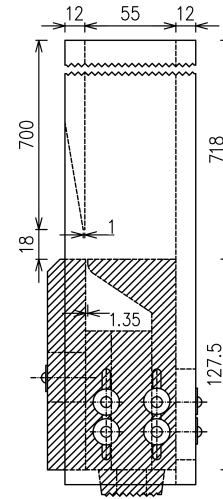


Fig. 2. Side view of the experimental pipe. The lengths are in milimeters.

An example of the sound signal waveforms for both regimes is presented in Fig. 3. The recordings took place in an anechoic chamber.
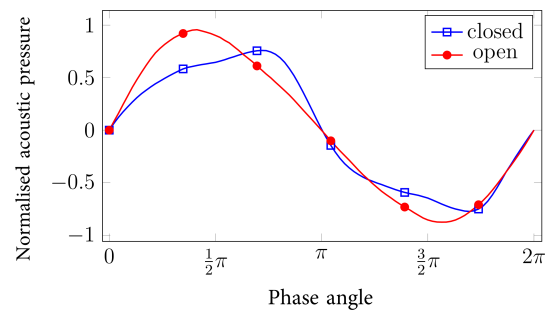


Fig. 3. Waveforms of far field acoustic pressure for closed and open pipe. The amplitudes are normalised so that the both signals have the same power. The markers correspond to the instants at which the PIV phases depicted in Fig. 5 were taken.

Schematics of the PIV setup along with the instruments used are presented in Fig. 4. All PIV data were
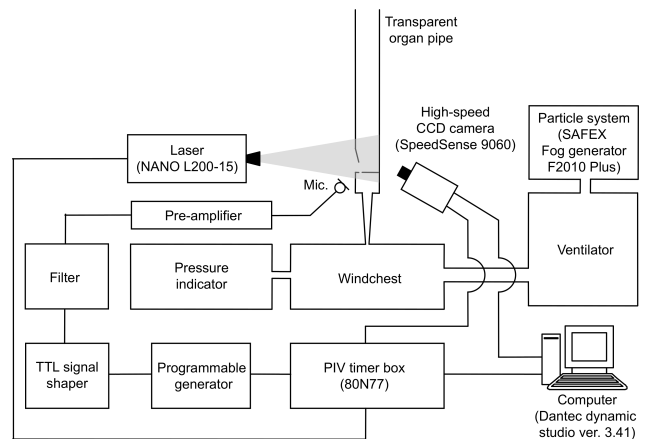


Fig. 4. Schematics of the PIV setup.

obtained by the phase locked method, well described e.g. in (Hruška, Dlask, 2017; Mickiewicz, 2015; Yoshikawa *et al.*, 2012). The sound signal served as a reference for the synchronisation and the PIV images were captured in 36 phases equidistantly dividing the period. A vector map of each phase was an average of 50 realisations (i.e., 50 snapshots of the unsteady flow with the same phase delay). For a detailed low level electrotechnical discussion of our measurement setup and instrumentation refer to (Guštar, Dlask, 2018). The PIV window has the dimensions of $54 \times 33$ mm (i.e., less than 5% of the fundamental sound wavelength).

The nebuliser fluid (Safex Normal Power Mix) produces particles of 1 μm diameter. The particle inertia and relaxation time were negligible at the system sounding frequency (see Vignola *et al.*, 1992; Melling, 1992).

It is useful to introduce some kind of analytical tool to investigate the raw airflow data obtained by PIV. In this article we employ the biorthogonal decomposition (BOD), a standard technique of turbulent flows data analysis, see e.g. (Uruba, 2012) for further reading, which has already been employed in the field of organ pipe aerodynamics (Mickiewicz, 2015; Hruška, Dlask, 2017).

The BOD decomposes the velocity field $u(\mathbf{x}, t_n)$ taken at the discrete time instants $t_n$ into a set of linked orthogonal modes in space $\varphi$ (topos) and time $\psi$ (chronos):

$$u(\mathbf{x}, t_n) = \overline{u} + \sum_{k=1}^{N} \lambda_k \varphi_k(\mathbf{x}) \psi_k(t_n), \qquad (2)$$

where $\overline{u}$ is a cycle averaged velocity, $N$ is the number of PIV snapshots ($N = 36$ in our case), $\lambda_k^2$ is the $k$-th eigenvalue of a covariance matrix $C_{ij}$ (a special treatment is necessary for complex valued quantities but this is not the case).

The covariance matrix $C_{ij}$ is defined:

$$C_{ij} = \frac{1}{N} \sum_{r=1}^{X} \sum_{s=1}^{Y} u(x_r, y_s, t_i) u(x_r, y_s, t_j), \qquad (3)$$

where $\mathbf{x} = (x_r, y_s)$, $X$, $Y$ are the analysed field spatial coordinates and their limits, $i, j = 1, ..., N$. The eigenvectors of $C_{ij}$ are the chronoses $\psi_k$. The corresponding toposes $\varphi_k$ are subsequently calculated

$$\varphi_k(\mathbf{x}) = \sum_{i=1}^{N} u(\mathbf{x}, t_i) \psi_k(t_i). \qquad (4)$$

When the modes are ordered according to their eigenvalues the most energetic flow phenomena are likely to be contained in the first few modes. When the measured phenomenon exhibits some sort of periodicity the chronoses tend to resemble a sequence like

$\sin x$, $\cos x$, $\sin 2x$, $\cos 2x$ ... (recall that the modes are pairwise orthogonal).

In order to assess the modes importance and overall quality of the decomposition the cumulative energy $CE$ is defined:

$$CE(k) = \frac{\sum_{j=1}^{k} \lambda_j^2}{\sum_{i=1}^{N} \lambda_i^2}. \qquad (5)$$

It estimates a relative amount of the already decomposed signal energy when $k$ modes have been included. It follows that when $CE \rightarrow 1$ almost all flow energy has been decomposed.

The same procedure may be generalised to any measured quantity $q(\mathbf{x}, t)$ (as it is done for the pressure below – see Discussion).

The Line Integral Convolution technique (LIC) is employed throughout the article to visualise the measured airflow velocities (Cabral, Leedom, 1993). The colour scale is fixed everywhere (in the PIV phases as well as in the toposes) ranging from 0 to 14 m·s$^{-1}$.

## 3. Results

### *3.1. Pictorial analysis*

Let us start with a simple pictorial analysis which will be subsequently supported by the BOD results. The phases 1, 7, 13, 19, 25, and 31 (i.e., the full period divided into $\pi/3$ steps) are depicted in Fig. 5 for both open and closed configurations.

Values of the instantaneous sound phases corresponding to the depicted PIV phases are marked. The acoustic pressure data were obtained from a microphone placed outside the vortical flow and they were corrected regarding the retarded time. Note that this is only an estimation of the sound phase at the mouth since it does not account for the near field effects. In both cases the most outward striking jet corresponds to zero of the acoustic pressure as it should, since the jet oscillations are synchronised with the acoustic velocity.

The most noticeable difference between the open and closed pipes is the airflow assymetry. Significantly lower velocity values are observed inside the closed pipe or pointing towards its interior. It is natural given that the averaged mass flux into the closed organ pipe should be vanishing. Several other differences follow from this assymetry. Vortical structures are not convected inside the closed pipe as it is in the case ot the open one (see phases 25 and 31 in Fig. 5). No distinguishable vortex is formed outside the open pipe during the influx, only a small eddy just below the tip of the labium (see phase 19). The depicted phases suggest that the lateral speed of jet passing below the labium
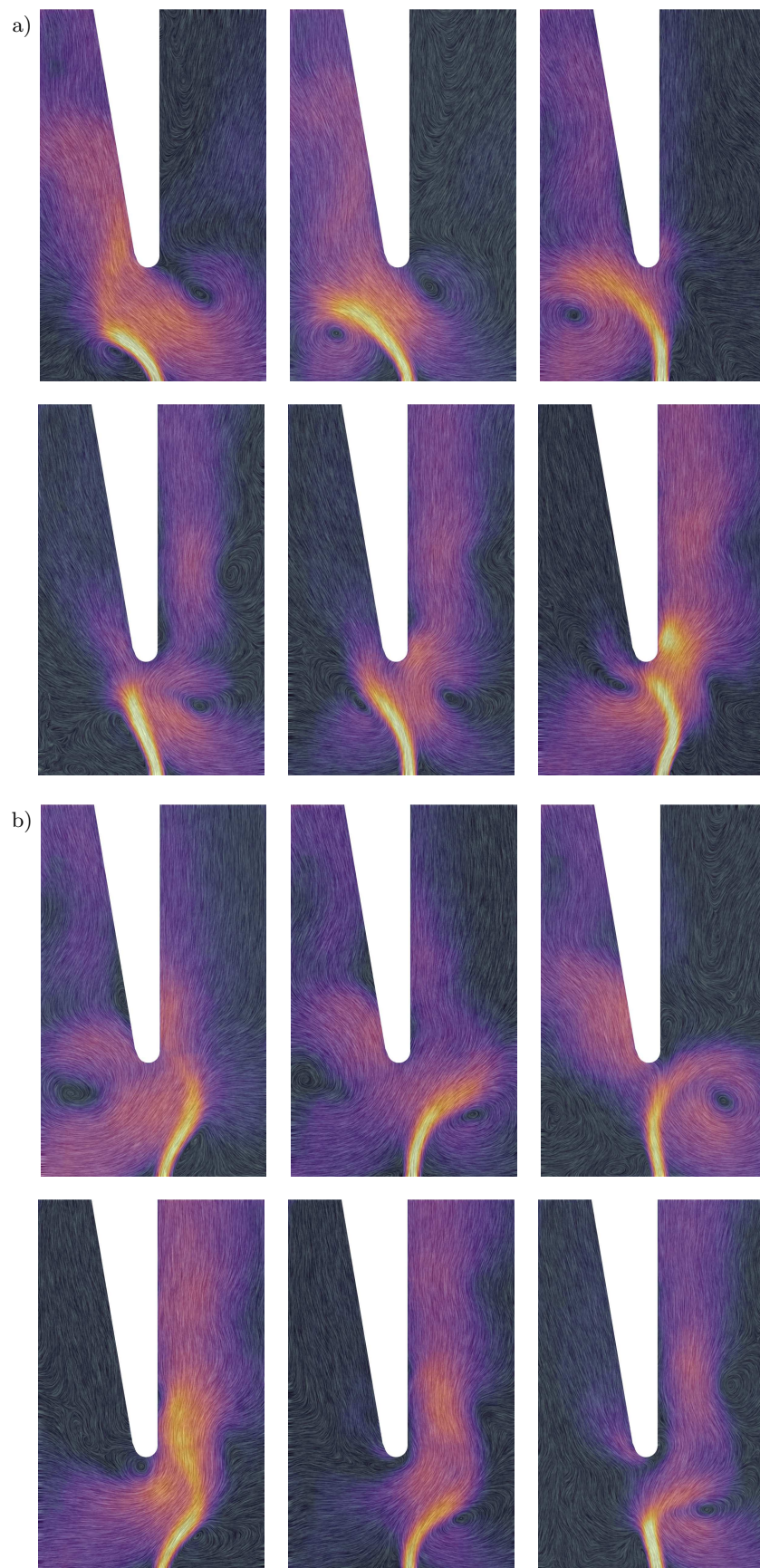
Fig. 5. Comparison of the phases 1, 7, 13 (a) and 19, 25, 31 (b). Within the sextuplets the closed configuration is always at the top and the open at the bottom.

is different. Specifically the jet seems to cross faster in the case of the closed pipe. This observation will be verified by the BOD below.

### 3.2. BOD analysis

First we should assess how many modes should be used to properly describe the unsteady velocity field. Such assessment relies on the cumulative energy defined by Eq. (5). The cumulative energies are listed in Table 2. It follows that using just two modes is enough and importance of the 2nd is much lower than that of the 1st one.

Table 2. Cumulative energies for the BOD decompositions of the open and closed pipe.

| $k$ | $CE$ open pipe | $CE$ closed pipe |
|---|---|---|
| 1 | 0.880 | 0.899 |
| 2 | 0.996 | 0.994 |
| 3 | 0.998 | 0.997 |
| 4 | 0.999 | 0.999 |

The mean velocity fields, the 1st and the 2nd topos and corresponding chronoses are depicted in Figs 6 and 7. The chronoses are normalised to have the maximum absolute value equal to 1 and the toposes are
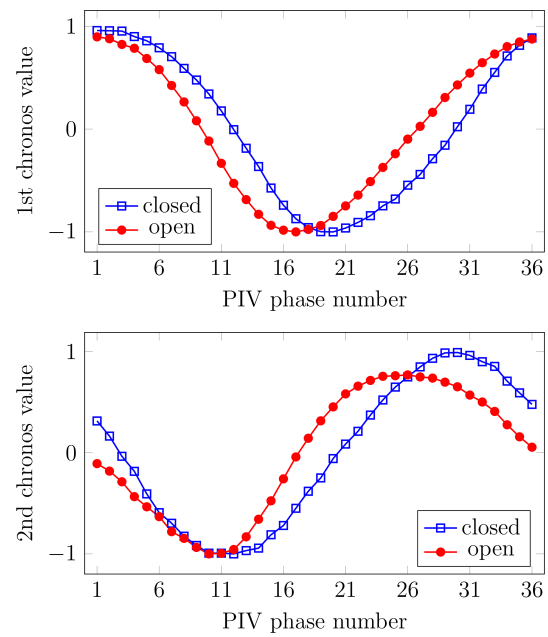


Fig. 7. 1st and 2nd chronoses of the closed and open organ pipes.

scaled accordingly counting in the contribution of the eigenvalues $\lambda$. So adjusted it is apparent that the contribution of the 2nd mode is less significant compared to the 1st one.
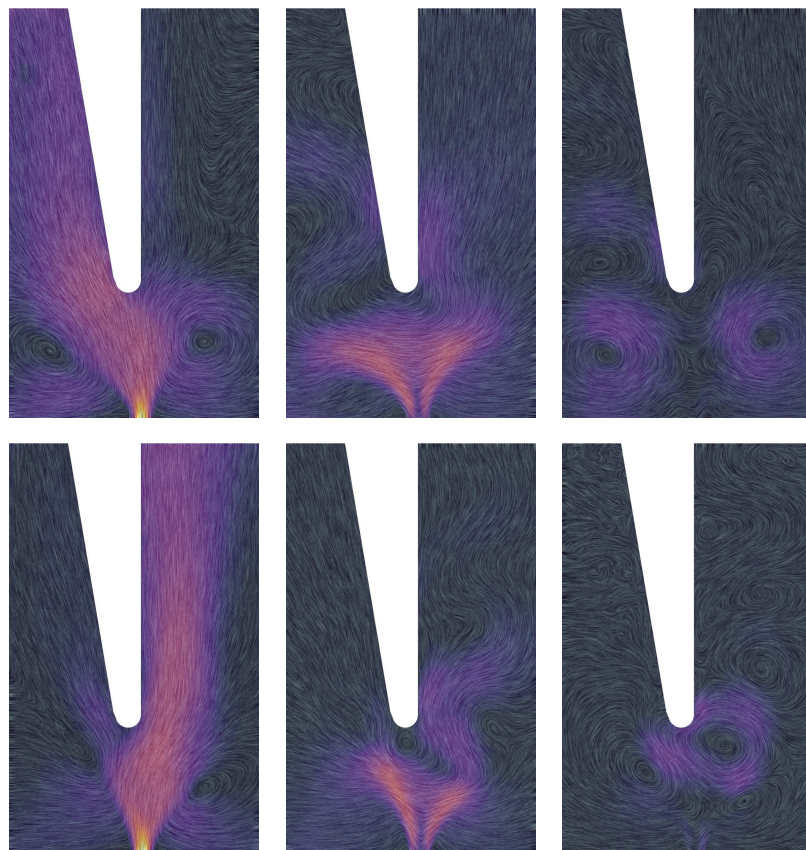


Fig. 6. Mean velocity fields (left column), 1st topos (middle column) and 2nd topos (right column) of the closed (top row) and open pipe (bottom row).

The mean velocity field shapes support the observation of the previous section: practically no averaged flux enters the closed pipe. The 1st mode shows the jet deflection extrema. The closed pipe jet is more inclined (see the 1st topos), its lateral motion is more abrupt and conversely the time spent in fully deflected state is prolonged (compare the 1st chronoses). Note that the closed pipe jet spends over one tenth of the period deflected outwards almost without lateral movement (see phases 36 and 1–3 of the 1st chronos). It corresponds to the rule of thumb that in the closed pipe case the acoustic velocities time evolution resemble a square wave. The large eddies governed by the 2nd mode are nearly symmetric in time and space for the closed pipe reinforcing or cancelling the eddies in the mean flow. In the case of the open pipe the large eddy next to the labium cancels the flow at the labium around phase 25 and conversely creates the fast flow adjacent to the labium at phase 13. However, recall that the contribution of the 2nd mode is quite weak (see Table 2).

Data from the subsequent modes show flow structures responsible for "sharpening the jet edges", i.e., marking a distinct boundary of the flow separation. They are generally less coherent and of lower kinetic energy (approximately 15 % of the whole snapshot). There are no significant qualitative differences between the open and closed pipes. Although the residual data exhibit quite low amount of kinetic energy they are still capable of changing the specific values of spatial derivatives of the velocity field (see Discussion). Neverthelles, the rate of cumulative energy growth on the next modes is slow in our case (Table 2) and adding more modes with low importance and unclear physical interpretation would not provide any closer insight.

## 4. Discussion

We would like to split Discussion into two distinct parts. The first would be a commentary to the experiment setup and results. Beside that we want to dedicate the second part of Discussion to the procedure of pressure assessment based on PIV since it is a highly intriguing way to be followed, although its use is currently rather a subject of discussion than the solid result in the field of edge aerophones acoustics (see below).

### 4.1. The experiment and results

The first concern is generality of the obtained results. The flow symmetry is dependent on the flue labium configuration so at least the open pipe behavior cannot be assumed fully universal. On the other hand, the substantial differences between closed and open pipe flow symmetries are likely to hold.

It has been shown (Hruška, Dlask, 2017) that the snapshots averaging within a PIV phase in order to obtain smoother data leads to faster growth of the cumulative energy but on the other hand to a "blurred jet" and the possibility of cancelling the vorticity as well.

An important drawback of employing the BOD as described above is that the decomposition based on the flow kinetic energy might not capture features crucial from the aeroacoustics point of view. Recall that the source terms in various aeroacoustic analogies depend rather on spatial derivatives of the velocity than the velocity itself (Uosukainen, 2011; Howe, 2002). Note for instance that the decisive 1st BOD mode of the open and closed pipe airflows does not differ substantially. It is natural since the velocity magnitudes of the jet are approximately equal and the oscillation takes place once in the sound period in both regimes. This problem is a subject of our future research. There are two major ways to be followed: either change the method, e.g. employ the oscillating patterns decomposition (Uruba, 2012) or change the input variable. An attempt for the latter is made in the next section.

Acoustic velocities are reported to be approximately one order smaller than the mean flow velocities (Chaigne, Kergomard, 2016), which makes them effectively inseparable if the experiment set up aims for the turbulent flow features. Note that due to the possible acoustic streaming from the strong acoustic field inside the pipe velocities are even weaker. Their effect scales with the second power of the acoustic Mach number, see e.g. (Červenka, Bednařík, 2016) for further details. Therefore, they are indistinguishable in the presented experiment and their contribution to the turbulent flow perturbations can be neglected in the studied scenario.

### 4.2. Pressure estimation

As it was mentioned before, the BOD analysis of the flow might not capture some traits important for aeroacoustics. We shall see that in order to bring the analysis closer to the sound production mechanism it is convenient to know the pressure distribution in the investigated domain, especially on the solid boundaries. In the presence of a stationary solid body (such as labium) in the flow, dipole sources emerge beside the free field quadrupolar contributions (Howe, 2002; Uosukainen, 2011). They are formally introduced by the so called Curle's aeroacoustic analogy – a direct extension of the well known Lighthill's analogy. Let $H$ denote the Heaviside step function defined as 0 for a point inside the solid body and 1 everywhere else. Let us suppose the low Mach and high Reynolds number limit. The wave equation for the pressure perturbations $p' = p - p_0$ then takes the form

$$\frac{1}{c_0^2}\frac{\partial^2}{\partial t^2}[Hp'] - \nabla^2[Hp'] = \nabla \cdot [\nabla \cdot (H\rho_0 \mathbf{uu})]$$
$$- \nabla \cdot [(p'\mathcal{I} + \rho_0 \mathbf{uu}) \cdot \nabla H], \quad (6)$$

where $\mathcal{I}$ is the identity tensor and $\mathbf{uu}$ is the dyadic product of the velocity vectors. It can be shown that the pressure term on the right hand side is the dominating one in the low Mach number limit (HOWE, 2002). Since it is nonzero only on the face of the body due to the $\nabla H$, it follows that the pressure exerted by the flow on the labium causing an unsteady force is of the key interest. Since the area of the PIV window is acousticaly compact we shall seek for the pressure instabilities related to the periodic flow motions.

The spatial domain of PIV measurement is small compared to the characteristic wavelength and the flow Mach number is small compared to unity. Hence we can assume the flow to be incompressible. The governing equations reduce to (BATCHELOR, 2000)

$$\frac{\partial \mathbf{u}}{\partial t} + (\mathbf{u} \cdot \nabla)\, \mathbf{u} = -\frac{1}{\rho_0}\nabla p + \nu \nabla^2 \mathbf{u}, \qquad (7)$$

$$\nabla \cdot \mathbf{u} = 0, \qquad (8)$$

where $\rho_0$, $p$, $\nu$ denote the ambient density, pressure, and kinematic viscosity, respectively. As the viscous boundary layer (neither acoustic nor turbulent) cannot be properly sampled in our PIV window and the input consists of averaged snapshots, the effects of viscosity and Reynolds stress distribution are neglected. Taking the divergence of Eq. (7) and using the property (8) we arrive at the the Poisson equation for pressure (DE KAT, VAN OUDHEUSDEN, 2011)

$$\nabla^2 p = -\rho_0 \nabla \cdot (\mathbf{u} \cdot \nabla \mathbf{u})$$

$$= -\rho_0 \left[ \left(\frac{\partial u_x}{\partial x}\right)^2 + 2\frac{\partial u_x}{\partial y}\frac{\partial u_y}{\partial x} + \left(\frac{\partial u_y}{\partial y}\right)^2 \right], \quad (9)$$

where the last expression is the source term in Cartesian coordinates. The Poisson equation must be supplemented with proper boundary conditions obtained from the momentum conservation equation evaluated at the boundary $\Gamma$. This leads to the Neumann boundary conditions in the form

$$\nabla p_\Gamma = -\rho_0 \left[ \frac{\partial \mathbf{u}}{\partial t} + (\mathbf{u} \cdot \nabla)\, \mathbf{u} \right]. \qquad (10)$$

Since the Eqs (9) and (10) contain the pressure only inside the differential operator it is necessary to set a fixed pressure value somewhere in the computational domain in order to obtain a unique solution and assure the numerical stability. This is the first obstacle that has to be overcome. We cannot be sure of the reference pressure based on the PIV measurement only. Note that the larger scale velocity variations influence the computational domain by the boundary conditions (10). The proper way of dealing with this problem would be placing a sensitive pressure probe inside the domain or at its boundary and synchronise it carefully with the PIV measurement.

The second weak spot lays in the finite precision of the PIV measurement and subsequent data treatment. Based on experiments with different interrogation areas and subsets of snapshots used for averaging we assess the relative uncertainty of the velocity components around 4%. However, it follows that the uncertainty of the spatial differences (needed for discretisation of the derivatives) might exceed 10% in many cases and the combined uncertainties in the right hand side of Eqs (9) and (10) can easily reach 25%. Therefore the data have to be preprocessed before solving the equations numerically.

We made an attempt to estimate the pressure by the aforementioned procedure. The BOD was used for smoothing the data in space and time. The flow field was reconstructed from the mean values, the first two modes, and in order to make the spatial derivatives more accurate two additional subsequent modes were included. The constant reference pressure was placed to the interrogation area with the least velocity variations (assessed by the 1st BOD mode). Nevertheless, the departures from the reference value due to the near field acoustic pressure were neglected by this choice. Equations (9) and (10) were discretised on the Cartesian mesh and solved by the successive over relaxation method (see e.g. PRESS *et al.*, 2007).

An interesting result was found for the closed pipe. The pressure field was decomposed by the BOD as well, and it followed from the cumulative energy that only one mode was important. The 1st chronos is depicted in Fig. 8. It turns out that the main unsteady process exhibits a waveform slightly resembling the odd harmonics features. It suggests that the 1st chronos is mainly influenced by the boundary velocities related to the large scale acoustic field rather than the source terms. The 1st pressure chronos maximum corresponds to the instant of jet transition from striking outwards the pipe to the inwards striking direction and vice versa. However, this topic should be studied in the future. See e.g. AUTERI *et al.* (2015); DE KAT, VAN OUDHEUSDEN (2011); VAN OUDHEUSDEN (2013) for further reading.
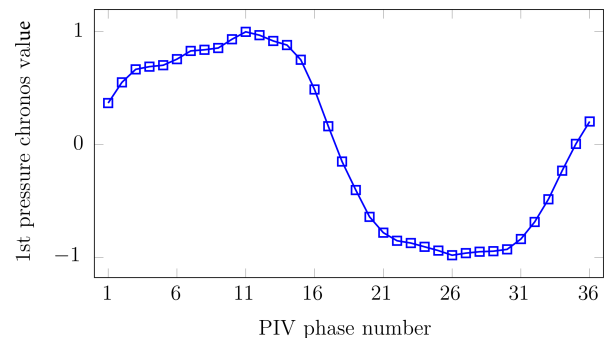


Fig. 8. 1st pressure chronos of the closed organ pipe.

## 5. Conclusions

The airflow in the mouth of the closed and open flue organ pipes was investigated by means of particle image velocimetry. Substantial differences were found in the mean velocity distribution and the lateral motion of the jet which subsequently caused a different behavior of the other flow coherent structures (such as vortex eddies). Some of the advantages and drawbacks of the biorthogonal decomposition application and the pressure assessment in this particular case were discussed which lead to a detailed proposition of the new tasks and problems to be solved.

## Acknowledgement

## References

1. AUTERI F. *et al.* (2015), *A novel approach for reconstructing pressure from PIV velocity measurements*, Experiments in Fluids, **56**, 45, 16 pages.

2. BAMBERGER A. (2008), *Vortex sound of the flute and its interpretation*, The Journal of the Acoustical Society of America, **123**, 5, 3239–3239.

3. BATCHELOR G.K. (2000), *An introduction to fluid dynamics*, Cambridge University Press, Cambridge.

4. CABRAL B., LEEDOM L. (1993), *Imaging vector fields using line integral convolution*, [in:] Proceedings of the 20th annual conference on Computer graphics and interactive techniques, SIGGRAPH '93, pp. 263–270, Anaheim, CA.

5. ČERVENKA M., BEDNAŘÍK M. (2016), *Variety of acoustic streaming in 2d resonant channels*, Wave Motion, **66**, 21–30.

6. CHAIGNE A., KERGOMARD J. (2016), *Acoustics of musical instruments*, Springer, New York, NY.

7. DE KAT R., VAN OUDHEUSDEN B.W. (2011), *Instantaneous planar pressure determination from PIV in turbulent flow*, Experiments in Fluids, **52**, 5, 1089–1106.

8. FABRE B., GILBERT J., HIRSCHBERG A., PELORSON X. (2012), *Aeroacoustics of musical instruments*, Annual Review of Fluid Mechanics, **44**, 1–25.

9. FLETCHER N., ROSSING T. (1998), *The physics of musical instruments*, Springer, New York.

10. GUŠTAR M., DLASK P. (2018), *Programmable generator of external triggering signal for dantec PIV timer box 80N77*, [in:] 2018 International Conference on Applied Electronics, 11–12 Sept., Pilsen, Czech Republic.

11. HIRSCHBERG A., RIENSTRA S.W. (2004), *An introduction to aeroacoustics*, Free online source, https://www.win.tue.nl/~sjoerdr/papers/les-swr-mh.pdf.

12. HOWE M.S. (1975), *The generation of sound by aerodynamic sources in an inhomogeneous steady flow*, Journal of Fluid Mechanics, **67**, 3, 597–610.

13. HOWE M.S. (2002), *Theory of vortex sound*, Cambridge University Press, Cambridge.

14. HRUŠKA V., DLASK P. (2017), *Connections between organ pipe noise and Shannon entropy of the airow: Preliminary results*, Acta Acustica united with Acustica, **103**, 1100–1105.

15. LIN D., POWELL A. (1998), *The scattering of hydrodynamic flow into sound by solid bodies – An alternative derivation of Howe's formula*, [in:] Proceedings of ICA, vol. 1, pp. 509–510, Seattle, USA.

16. MACDONALD R. (2009), *A study of the undercutting of woodwind toneholes using particle image velocimetry*, Doctoral Thesis, University of Edinburgh.

17. MELLING A. (1992), *Tracer particles and seeding for particle image velocimetry*, Measurement Science and Technology, **8**, 12, 1406–1416.

18. MICKIEWICZ W. (2015), *Particle image velocimetry and proper orthogonal decomposition applied to aerodynamic sound source region visualization in organ flue pipe*, Archives of Acoustics, **40**, 4, 475–484.

19. MIYAMOTO M. *et al.* (2013), *Numerical study on acoustic oscillations of 2D and 3D flue organ pipe like instruments with compressible LES*, Acta Acustica united with Acustica, **99**, 1, 154–171.

20. PRESS W.H., TEUKOLSKY S.A., VETTERLING W.T., FLANNERY B.P. (2007), *Numerical recipes. The art of scientific computing*, 3rd ed., Cambridge University Press, Cambridge.

21. UOSUKAINEN S. (2011), *Foundations of acoustic analogies*, VTT Publications, Helsinki.

22. URUBA V. (2012), *Decomposition methods in turbulence research*, EPJ Web of Conferences, **25**, 01095, 21 pages.

23. VAN OUDHEUSDEN B.W. (2013), *PIV-based pressure measurement*, Measurement Science and Technology, **24**, 3, 032001.

24. VIGNOLA J.F., BERTHELOT Y.H., JONES S., JARZYNSKI J. (1992), *Equation of motion of microparticles in suspension in an insonified medium*, Journal of Acoustical Society of America, **92**, 332–334.

25. YOSHIKAWA S., TASHIRO H., SAKAMOTO Y. (2012), *Experimental examination of vortex-sound generation in an organ pipe: A proposal of jet vortex-layer formation model*, Journal of Sound and Vibration, **331**, 11, 2558–2577.